ISSN 0023-1584, Kinetics and Catalysis, 2008, Vol. 49, No. 6, pp. 840–858. © Pleiades Publishing, Ltd., 2008.
Original Russian Text © T.G. Kuznetsova, V.A. Sadykov, 2008, published in Kinetika i Kataliz, 2008, Vol. 49, No. 6, pp. 886–905.

Specific Features of the Defect Structure of Metastable Nanodisperse Ceria, Zirconia, and Related Materials

T. G. Kuznetsova and V. A. Sadykov

Boreskov Institute of Catalysis, Siberian Branch, Russian Academy of Sciences, Novosibirsk, 630090 Russia
e-mail: tgkuzn@catalysis.nsk.su

Received March 28, 2008

Abstract—Models of the defect structure and microstructure of the CeO_2, ZrO_2, Ce–Me^1–O (Me^1 = La, Sm, Zr), and Zr–Me^2–O (Me^2 = Ca, Sr, Ba) nanomaterials are discussed. For ceria-based fluorite, the appearance of weakly bound oxygen and the mobility of bulk oxygen are due to distortions in the Ce–O coordination sphere and the appearance of interstitial oxygen atoms. For pure and doped zirconia, the phases forming in the intermediate temperature range are characterized by metastable structural networks differing from those observed in the equilibrium phases. The change in the local environment of the Zr cations (eight-atom coordination sphere) from a square antiprism in the initial salts to a distorted fluorite-like polyhedron in zirconia and the principle of structural conformity between hydrolyzed cations and the terminal hydroxyls of the Zr complexes in solution are the factors determining the genesis and structural features of the metastable phases. The defect structure and microstructure of the complex fluorite-like oxides have an effect on the state of the supported active component, favoring the formation of clustered species in the vicinity of extended defects in the support. Some examples of this effect in different types of reactions are provided.

DOI: 10.1134/S0023158408060098

Ceria and zirconia are widely used as supports and structural and electronic promoters for enhancing the activity, selectivity, and thermal stability of catalysts [1]. The most important application area of cerium-containing materials is redox processes, for the fluorite structure of ceria can withstand high levels of oxygen nonstoichiometry without changing its structural type. These materials have been investigated most comprehensively abroad as three-way automotive catalysts. In spite of the numerous studies carried out in this field, the structural features and defectiveness of ultrafine ceria and zirconia and related materials and their dependence on the preparation method have not been elucidated in sufficient detail. Because of the widening of the variety of reactions to which these systems might be applicable (hydrocarbon and CO oxidation and organic synthesis), these aspects should not be ignored.

Here, we will discuss models of the defect structure of nanosized CeO_2, ZrO_2, and mixed oxides based on them, namely, Ce–Me^1–O (Me^1 = Zr, La, Sm) and Zr–Me^2–O (Me^2 = Ca, Sr, Ba) prepared by coprecipitation and polymerized organometallic complex (POC) methods [2]. These materials have been characterized in detail by X-ray diffraction, TEM, IR spectroscopy, Raman spectroscopy, SAXS, DRS, and EXAFS [2–13]. We will provide examples illustrating the effect of defect structure on the state of supported active components and on their properties in the selective catalytic reduction (SCR) of NO_x, methane oxidation into synthesis gas, water–gas shift reaction (as applied to fuel cells), and limonene diepoxide conversion. We will summarize the studies supported by Russian and foreign grants in 1999–2005.

PURE CERIA AND ZIRCONIA

CeO_2

CeO_2 forms an fcc lattice (space group *Fm*3*m*, fluorite type). In this structure (Fig. 1), each cerium cation is surrounded by eight equivalent oxygen anions located in the corners of a cube [1]. Each oxygen anion is tetrahedrally coordinated to four cerium cations. The fluorite structure has well-defined octahedral holes into which oxygen can be displaced from its regular position to form interstitial oxygen (IO), which is a Frenkel defect. This type of defect, along with the formation of an anionic vacancy, is energetically most favorable. The removal of oxygen from perfect CeO_2 is a highly energy-consuming process requiring at least 800–900 kJ/mol [14]. The formation of a defect cluster (displacement of part of the oxygen anions from their regular positions) lowers the energy barrier to oxygen desorption. Declining in its oxygen stoichiometry, CeO_2 forms a number of oxygen-deficient phases of variable composition, Ce_nO_m, which result in the relaxation of the fluorite structure [1]. At a low oxygen nonstoichiometry, one anionic vacancy (Ce^{3+}) can be compensated for by a shift of six octants or more (Fig. 1), producing a complex defect. Various preparation proce-

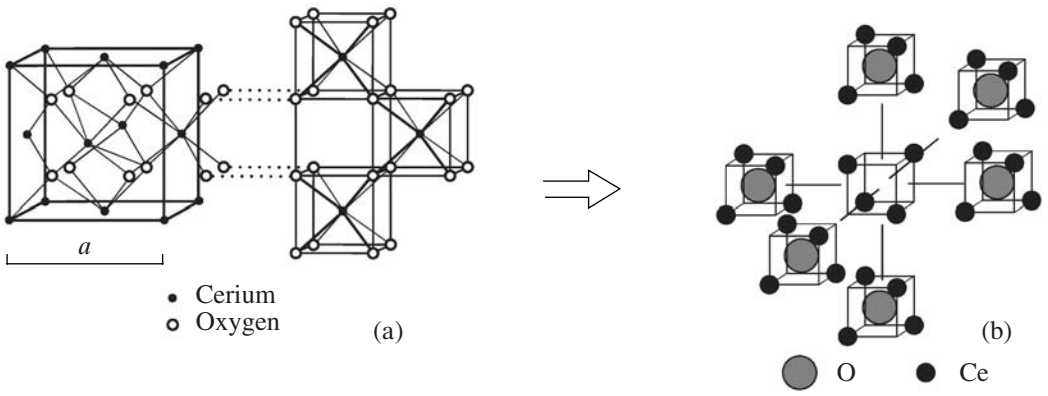

Fig. 1. (a) Fluorite structure of CeO_2 and (b) one of the variants of anionic vacancy compensation—coordination defect including an oxygen vacancy surrounded by an ensemble of six nearest-neighbor octants [1].

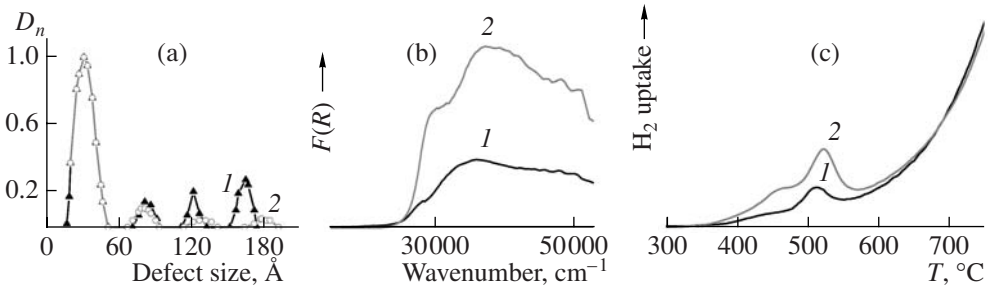

Fig. 2. (a) Defect size distribution (SAXS data), (b) diffuse reflectance spectra, and (c) H_2 TPR spectra for CeO_2 prepared by (*1*) cerium nitrate decomposition (S_{sp} = 3 m^2/g) and the POC method (S_{sp} = 19 m^2/g). T_{calcin} = 700°C.

dures and cerium sources have been tested in CeO_2 synthesis [1]. With inorganic sources of cerium, calcination at 500°C yields CeO_2 with S_{sp} = 100–150 m^2/g [15]. Addition of a surfactant at the synthesis stage allows the specific surface area to be increased to 200 m^2/g [16]. The high stability of the cationic sublattice of the dioxide ensures the formation of the fluorite structure, no matter what the synthetic procedure. However, an attempt to achieve a higher degree of dispersion of the oxide can result in the stabilization of Ce^{3+} cations, whose concentration increases significantly as the particle size decreases below 100 Å. In this case, charge compensation can be due to the formation of surface O_2^{2-} species [17]. Although no cerium sesquioxide phase has been detected by X-ray diffraction in CeO_2 synthesis, there can be residual Ce^{3+} cations when cerium(III) nitrate is used as the source of cerium, and they can appear during heat treatment as well. These cations affect the defect structure of fluorite by forming extended defects. These defects are very stable because the mobility of cerium ions is significant only above 800°C.

CeO_2 was synthesized by cerium nitrate decomposition and by the POC methods. The latter includes the formation of chelate-like compounds of metal cations (from aqueous salt solutions or crystalline hydrates) with citric acid–ethylene glycol esters. Subsequent heating of these compounds under oxygen-deficient conditions results in the formation of a polymer and then a complex carbon-containing matrix. Controlled oxidation of this matrix yields the oxide starting at 300°C. Optimization of the POC synthesis [2] has demonstrated that this method can be successfully used in the preparation of fine-particle mixed oxides (complex Ce- and Zr-containing materials and perovskites) [2–4, 8].

According to X-ray diffraction data, CeO_2 prepared by these methods at 700°C is fluorite with the same unit cell parameter of a = 5.411 Å and a coherent-scattering domain size of 1000 and 500 Å, respectively. At a residual Ce^{3+} content of <1% (according to magnetic susceptibility data obtained by the standard Faraday technique [2]), the product does not contain the sesquioxide phase. The trivalent cerium cations generate extended defects (Fig. 2a). These are probably located near microdomain boundaries, because, as S_{sp} increases, their size decreases (Fig. 2a), while their total intensity increases from 20 to 160 arb. units. According to EXAFS data, this leads to the occurrence of two Ce–O distances (2.240 and 2.390 Å [4]) versus a single Ce–O distance (2.343 Å) in cerium dioxide calcined at

1300°C [18]. For the space group $Fm3m$, a single vibration must be Raman-active (F_{2g}, 465 cm^{-1}) and one triply degenerate vibration split into transverse and longitudinal optical modes must be IR-active (F_{1u}, 272 and 595 cm^{-1}). Symmetry reduction or the polycrystallinity of the sample will further complicate the spectra [19]. The Raman spectrum of CeO_2 shows, along with a strong band at 463 cm^{-1}, weak bands at ~400 and 500 cm^{-1}, which are observable when the spectrum is recorded on an enlarged scale [3]. The broadening of the IR spectrum of CeO_2 [3] caused by a decrease in the particle size indicates that structure distortions take place [19]. This is accompanied by an increase in the concentration of hydrogen-bonded hydroxyls from 3 to 8 arb. units (absorption band at ~3400 cm^{-1}).

The electronic spectra of ceria are very sensitive to the coordination environment of the cerium cations: the absorption edge shifts to longer wavelengths as the symmetry or the coordination number (CN) decreases [20, 21]. The diffuse reflectance spectrum exhibits a Ce^{4+}–O^{2-} charge-transfer band at ~37000 cm^{-1} and an extra band at 28000–30000 cm^{-1}, whose intensity grows with an increase in S_{sp}. This band can arise from structure distortions. These distortions lower the energy barrier to oxygen removal, causing the appearance of weakly bound oxygen (Fig. 2c). A strong low-temperature reduction peak was also observed foe CeO_2 synthesized from $(NH_4)_2Ce^{4+}(NO_3)_6$ with a large S_{sp} value (170 m^2/g) and a smaller particle size (~50 Å) [22]. In this case, although a Ce(IV) salt is used, the formation of extended defects is due to either the partial reduction of the cerium cations or the small particle size.

Thus, the most abundant defects in CeO_2 are extended defects with an effective size of about 20–40 Å that occur at microdomain boundaries and are structurally organized as the nonstoichiometric oxides Ce_nO_m (Fig. 1). The electroneutrality of the latticed is ensured by the stabilization of OH groups on the reduced cerium cations. The defect concentration depends on the synthesis method and increases as the particle size of CeO_2 decreases. Even a low vacancy (Ce^{3+}) concentration causes the formation of a defect module up to the appearence of an extended defect. The occurrence of a longer Ce–O bond (2.39 Å) implies the presence of weakly bound oxygen. The shorter Ce–O bond (2.24 Å) is likely due to structure distortions rather than interstitial oxygen (IO) formation.

ZrO_2

ZrO_2 forms several polymorphic modifications. Thermodynamically, the most stable of them is the monoclinic modification (M), which turns into the tetragonal modification (T) at ~1200–1500°C. The cubic modification (C) forms only near the melting point (~2400°C). The phases T and C have a fluorite structure with corner-sharing coordination polyhedra, and the M-phase has a baddeleyite structure in which part of the coordination polyhedra are edge-sharing. As a consequence, this phase has two types of alternating anionic networks consisting of either tetrahedral or trigonal oxygen. The samples calcined at medium temperatures contain the phase T or C along with the phase M, and their proportions depend on the synthesis method and conditions and on the starting zirconium salt. This finding was long discussed in the literature. The stabilization of the phase T or C and their transformation into the phase M were attributed to energy factors, to the formation of the phases M and T/C from different precursors, and to the effect of defects [23–30]. It was assumed that the phase M forms from a more hydrated precursor of ZrO_2 (tetramers joined in a sheetlike fashion) in zirconium oxychloride (ZOC) ageing in acid solutions, while the fine-particle phase T forms from tetramers joined in a rodlike fashion in precipitate ageing in alkali solutions. Various types of defects, namely, anionic and cationic vacancies, extralattice zirconium cations, and Schottky defects (zirconium cationic vacancy plus two anionic vacancies) were observed in nanodisperse ZrO_2 [26–28, 31–34]. However, these data did not allow the effects of these defects on the stabilization of the phases T and C and on their transformation into the phase M to be analyzed. The low-temperature phases T and C can be stabilized by introducing low-valence cations, which decrease the unit cell parameter ratio c/a (tetragonality) and partially eliminate the internal strain of the lattice [10, 20, 35–37]. No theory of this stabilizing effect has been developed, but it is believed that significant factors in stabilization are the cation content and radius and the presence of oxygen vacancies.

In order to understand the causes of the stabilization of the low-temperature phases T and C, it is essential to consider the structures of the most common zirconium salts—zirconium oxynitrate (ZON) and ZOC—and zirconium polyhydroxo complexes that form upon the dissolution of these salts in water. The first salt consists of infinite double $(Zr(OH)_2NO_3(H_2O)_2)_n^{n+}$ chains, in which each zirconium cation is dodecahedrally coordinated to four hydroxyls, two water molecules, and one nitrate ion [38]. These chains are linked together by hydrogen bonds through extra water molecules and nitrate groups located between the chains. As for ZON, it was found that dimer species joined in a rodlike fashion (double chains) form in acid media (according to SAXS data) [39]. ZOC consists of $[Zr_4(OH)_8(OH_2)_{16}]^{8+}$ tetramers forming a coordination dodecahedron, and the Cl^- anions are not bonded directly to these tetramers [40, 41]. The zirconium cation in the tetramer is surrounded by eight oxygen anions arranged as a square antiprism, of which four belong to bridging hydroxyls and are located in the vertices of a cube and the other four belong to terminal hydroxyls/water molecules and are displaced from the fluorite positions to the cube edges (Fig. 3a). The tetramer structure persists upon the dissolution of the salt in water, but its longest $Zr–OH_2$ bonds can consecutively liberate a proton and the

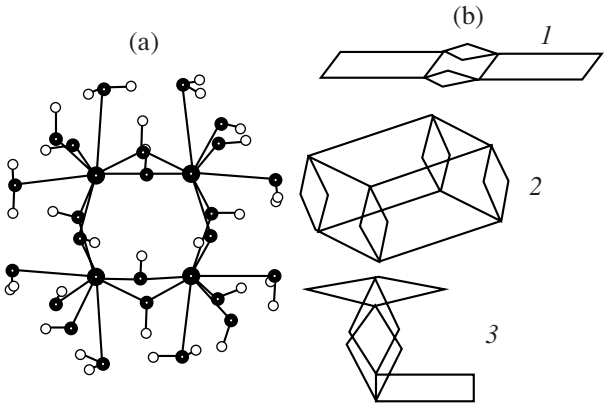

Fig. 3. (a) Structure of the Zr_4 $(\mu\text{-}OH)_8(H_2O)_8(OH)_8$ tetramer and (b) some variants of the joining of the planar tetramers into (*1*) sheetlike, (*2*) rodlike, and (*3*) displaced rodlike structures [5, 6].

resulting OH groups can cause further polymerization/condensation. The degree of polymerization increases with an increase in pH. The tetramers can join through terminal hydroxyls to yield a sheetlike (ribbonlike) or a rodlike structure (Fig. 3b). It is also possible that, in the rod, two tetramers are displaced relative to one another by 45° in one plane. Calculations demonstrate that these structures are equiprobable [5]. The SAXS spectrum of fresh and aged aqueous solutions of ZOC has several inflections, indicating the existence of a size distribution and, possibly, a geometry distribution for the zirconium hydroxo complexes [6, 9]. Processing of the SAXS data in terms of particle size (diameter) distribution has indeed demonstrated the existence of particles of different sizes (Fig. 4a). The characteristic size of the zirconium hydroxo complexes (width of the main peak) depends on the ZOC concentration, the type of the alkaline-earth metal (AEM) cation, the ageing conditions, and the way of preparing the starting solution. Raising the zirconium salt concentration or introducing an AEM cation leads to an increase in the observed particle size from 15–30 to 50 Å. Larger particles are also observed, whose proportion is particularly significant after ageing at an elevated temperature for both the pure ZOC solution and the same solution containing Sr cations (Fig. 4b). The size distribution of the large particles definitely has a discrete character characteristic of ribbon structures (according to estimates of the radius of gyration).

According to EXAFS data, the Zr–O and Zr–Zr distances in the starting ZOC solution [6, 9] indicate a distorted tetramer structure: along with the averaged Zr–O distance of 2.21 Å, three different Zr–Zr distances (3.34, 3.69, and 4.91 Å) are observed, which correspond to the sides and the diagonal of a distorted square [40] and coincide satisfactorily with the side (3.56 Å) and diagonal (5.0 Å) of the regular square in the ZOC crystal [41]. This suggests that there is weak interaction between tetramers, which is likely due to hydrogen bonding. Significant changes in the tetramer structure take place only in the solutions aged at an elevated temperature (80°C), including those containing AEM cations. In this case, the Zr–O distance is shortened from 2.21 to 2.19 Å and a single Zr–Zr distance (3.52–3.55 Å) corresponding to the side of a regular square is observed. The small coordination numbers for this distance, particularly in the presence of Sr or Ba cations, may be evidence that the plane of the square is distorted more severely.

Thus, depending on the ZOC concentration, aqueous ZOC solutions form aggregates with a dominant size up to 20–60 Å. These aggregates consist of several tetramers, which are joined in ribbonlike and rodlike fashions and interact weakly. This type of structural organization can be detected owing to the formation of an outer layer of chloride counterions (similar to the electrical double layer) counterbalancing the charge of the aggregate. AEM (Ca, Ba) cations, which are octahe-

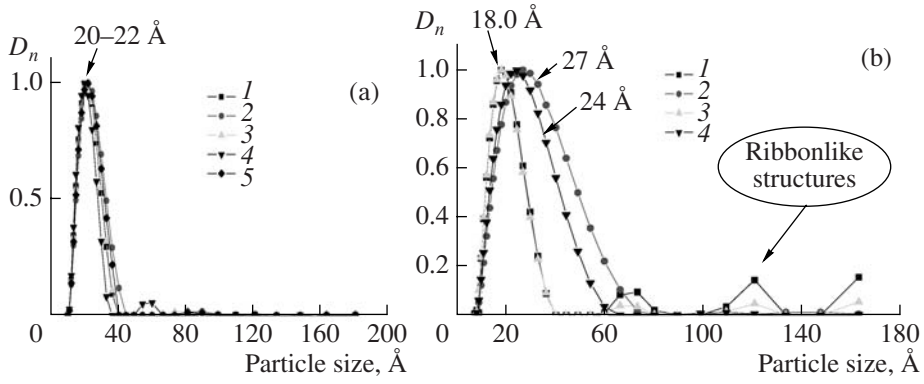

Fig. 4. Particle size distribution for (a) initial and (b) aged (80°C) zirconium oxychloride solutions doped with Ca, Sr, and Ba cations and zirconium acetate solutions (according to SAXS data). (a): (*1*) 0.1 M Zr (ZOC), (*2*) 0.1 M Zr + 0.011 M Ca, (*3*) 0.1 M Zr + 0.011 M Sr, (*4*) 0.1 M Zr + 0.011 M Ba (after 3 days), and (*5*) 0.1 M ZAc. (b): (*1*) 0.1 M Zr, (*2*) 0.1 M Zr + 0.03 M Ca, (*3*) 0.1 M Zr + 0.03 M Sr, and (*4*) 0.1 M Zr + 0.03 M Ba.

Table 1. Influence of the solution and precipitate ageing conditions on the properties of ZrO_2 synthesized from zirconium oxychloride and calcined at 500°C

Sample no.	Synthetic procedure	S_{sp}, m^2/g	Coherent-scattering domain size for the phases M and T, Å	Phase M fraction, %
1	Commercial ZrO_2	35	500	100
2	Ageing of a 0.1 M solution at pH ~2.0 and 100°C for 50 h followed by precipitation with NH_4OH at pH 10.3	73	75/50	80
3	Ageing of a 0.5 M solution at pH ~1.3 and 100°C for 50 h followed by precipitation with NH_4OH at pH 10.3	81	70/100	60
4	Ageing of a 0.5 M solution at pH ~1.3 and 100°C for 175 h followed by precipitation with NH_4OH at pH 10.3	91	100/75	70
5	Ageing of freshly precipitated zirconium hydroxide (0.5 M) at T_{room} and pH 10.3 for 250 h under stirring	120	70/95	50
6	Ageing of freshly precipitated zirconium hydroxide (0.5 M) at T_{room} and pH 10.3 for 250 h without stirring	94	–	–
7	Ageing of freshly precipitated zirconium hydroxide (0.5 M) at T_{room} and pH 10.3 in the light of a broadband Hg lamp for 12 h under stirring	74	100/<50	90
8	Ageing of freshly precipitated zirconium hydroxide (0.5 M) at 100°C and pH 10.3 for 50 h without stirring	150	75/70	40
9	Ageing of freshly precipitated zirconium hydroxide (0.5 M) at 100°C and pH 10.3 for 175 h without stirring	196	<50/60	10

drally coordinated by water molecules in aqueous solutions [42], can be localized between terminal hydroxyls/water molecules of nearest-neighbor rodlike association species (according to the structure conformity principle) to form weak electrostatic bonding favorable for the stabilization of the rods. Strontium cations, which form more complicated structures with water molecules (having a CN of ≈ 9) [42], are most likely localized between planar tetramers, thus favoring the stabilization of ribbonlike and sheetlike association species. The interaction between the tetramers can be enhanced by forced hydrolysis. These inferences are confirmed by data concerning the design of pillared clays containing ZrO_2 nanopillars [5–7, 9, 43], which are synthesized using ZOC solutions. The difference between the structural organizations of weakly bonded polyhydroxo complexes in a pure ZOC solution and the same solution containing an AEM cation provides makes it possible to control montmorillonite pillaring and thereby obtain material with different properties.

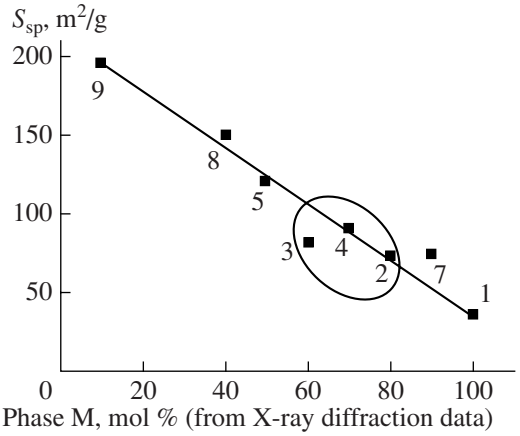

Fig. 5. Influence of the ageing conditions on the S_{sp} and percentage of the phase M of ZrO_2 (500°C). The samples are numbered as in Table 1.

The existence of weak interaction between tetramers in the solution even after ageing is confirmed by the strong dependence of the phase composition, coherent-scattering domain size, and S_{sp} of ZrO_2 (Table 1) on the synthesis (precipitation) conditions. This is particularly true for precipitate aging at high pH values, indicating that the precipitated zirconium hydroxide is highly labile. The data presented in Table 1 reveal a linear dependence of S_{sp} on the fractions of the phases M and T (Fig. 5). Extrapolation of S_{sp} to 100% phases M and T gives S_{sp} = 40–50 and ~200 m^2/g, respectively. The samples containing >50% phase M show deviations from proportionality. The causes of these deviations will be elucidated below when considering the defect structure.

For the standard precipitation procedure using a base, M : T = 1 : 1. If the sheetlike (ribbonlike) and rodlike structures are the precursors of the phases M and T, respectively, there ration in the solution also must be 1 : 1. The fraction of the phase M is larger for the ageing of a dilute solution and is smaller for a concentrated solution, but it increases as the duration of ageing at 100°C is extended. As this takes place, the particle size

Table 2. Effects of the synthetic procedure and the calcium cation content on the S_{sp} and phase composition of ZrO_2 calcined at 700°C for 2 h

Sample no.	Chemical composition*	Synthetic method	S_{sp}, m^2/g	Phase composition/coherent-scattering domain size, Å
1	ZrO_2	POC	8	70% M/310 + 30% T/200
2	2.4CaO–ZrO_2	CZON	165	T/80
3	5.0CaO–ZrO_2	POC	72	T or C/50
4	10.0CaO–ZrO_2	CZON	60	T or C/60

Note: Synthetic methods: POC = Polymerized organometallic compound method using zirconium oxychloride; PZON = precipitation from zirconium oxynitrate (prolonged ageing) [10].
* The amount of introduced CaO is in mol %.

of the phase M increases and that of the phase T decreases, which is in agreement with the fact that ageing increases the fraction of large discrete association species whose structure consists of ribbonlike/sheetlike units (Fig. 4b). The increase in the percentage of the phase T during the ageing of the hydroxide precipitate at an elevated temperature is attributed to the increase of x in the formula $\{ZrO_x(OH)_{4-2x} \cdot yH_2O\}_n$ via olation- and oxolation-type reactions [25]. The high lability of the precipitate with respect to UV radiation and other random factors at lower temperatures can be due to the mere removal of weakly bonded hydroxyls (water molecules). This results in a larger fraction of the phase M, suggesting that the residual (weakly and strongly bonded) hydroxyls play an important role in the formation of the phase composition and S_{sp} of ZrO_2.

Zirconia resulting from POC synthesis (in which the amount of water is smaller than in the precipitation method) is dominated by the phase M with a small S_{sp} (Table 2). The introduction of Ca ions favors the formation of the phase T or C with a small particle diameter (Table 2). The unit cell parameter of the calcium-doped samples (5–10 mol % Ca) is 5.12 Å and is independent of the promoter content. This possibly means that Ca is the structure-forming cation preventing the formation of large ribbonlike and sheetlike association species (as in the case of the polyhydroxo complexes in solution). For comparison, consider the sample with the lowest Ca cation content [10] (Table 2), which was identified as the phase T with a doubled unit cell parameter (10.23 Å, as in the case of Ba cations). As was mentioned above, a perovskite-like layered structure forms in the presence of Sr cations. These data are in full agreement with the data obtained for ZOC solutions containing AEM cations. Occupying positions between rodlike structures, Ca and Ba cations favor the formation of a more symmetrical structure. Its formation also requires that the local surrounding of the zirconium cations be changed from the square antiprism to a fluorite-like polyhedron. The introduction of Sr cations increases the proportion of ribbonlike structures (Fig. 4b). An increase in the symmetry of undoped ZrO_2 is achievable only by prolonged ageing of the hydroxide precipitate at an elevated temperature.

The stabilization of the phases T and C in going away from equilibrium conditions and the noticeable effect of small amounts of promoters on this process indicate a metastable organization of these phase in which a significant role cam be played by defects (residual hydroxyls, oxygen vacancies, and trigonal oxygen). In order to elucidate their role, we studied zirconia samples by IR and Raman spectroscopy and DRS. The irreducible representations of the optical modes of different ZrO_2 modifications [20] indicate that the optical spectrum of the phase C is simple, with one Raman-active vibration and one IR-active vibration. Symmetry reduction causes an increase in the number of active modes: for the phase T, there are six Raman-active modes and three IR-active modes; for the phase M, 18 and 15, respectively. The IR spectra of ZrO_2 samples prepared under different ageing conditions are presented in Fig. 6a in the order of decreasing phase M percentages. The spectra of all these samples have a complicated contour and exhibit absorption bands typical of the phase M. The intensities of these bands decrease as the phase T content increases. For the perfect phase M, there must be well-defined splittings (doublets) of the tetragonal bands near 435 (445–415) and 365 (375–360) cm^{-1} and narrow absorption bands at 740, 270, and 235 cm^{-1} [44]. The IR spectra presented here contain broad absorption bands, which are evidence that the structure of the phase M has distortions, which are due to, inter alia, the small particle size of this phase. As the percentage of the phase M decreases (in the 50–70% range), the intensities of the most characteristic bands decrease nonlinearly. The IR spectrum of the sample dominated by the phase T differs from the IR spectra of the Ca-doped samples even at low promoter contents (Fig. 6b). The structure of the phase M actually differs significantly from the structures of the phases T and C. In the phases T and C, the zirconium cations are located in the centers of cubes ($CN_{Zr-O} = 8$) and the O^{2-} ions are in a tetrahedrally surrounded by zirconium cations. In the phase M ($CN_{Zr-O} = 7$), half of the oxygen atoms have a heavily distorted tetrahedral environment characterized by three different Zr–O distances and the other half of the oxygen atoms have a a planar trigonal environment

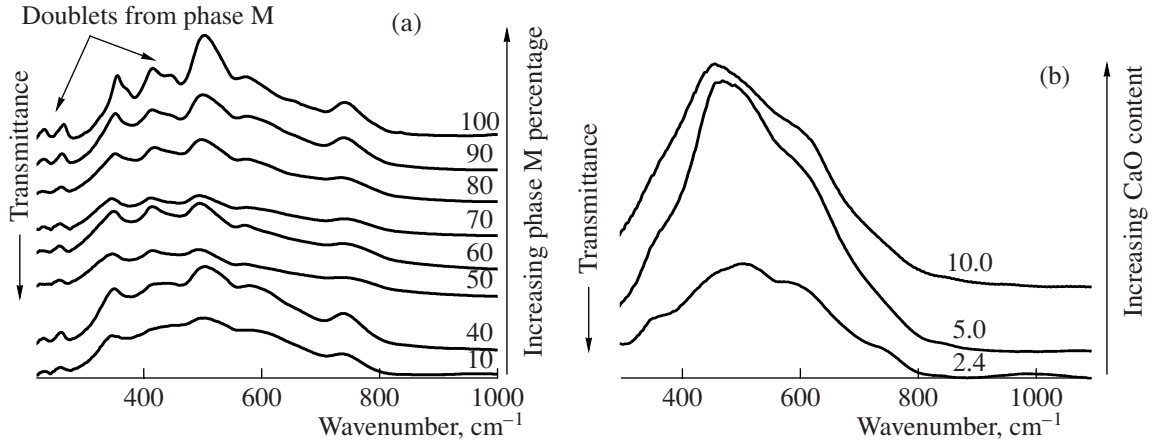

Fig. 6. (a) IR spectra of ZrO_2 prepared by precipitation (arranged in the order of increasing phase M percentages). (b) IR spectra of ZrO_2 doped with calcium cations. Figures 6a and 6b refer to samples from Tables 1 and 2, respectively.

[45]. The absorption band at 780 cm^{-1} was assigned to asymmetric vibrations of oxygen in the planar triangle OZr_3 [20]. In our case, this band occurs at 740 cm^{-1}. As the percentage of the phase M decreases, this band, like the other band characteristic of the phase M, weakens and its contour becomes more diffuse, indicating that the phase M is disordered, particularly at high percentages of the phase T.

The Raman spectra obtained using an Nd–YAG laser (Fig. 7) can be helpful in the identification of only the phase M, because the phases T and C do not absorb visible light, as follows from DRS data (Fig. 8a). The Raman spectra arranged in the order of decreasing phase M percentages indicate the presence of only this phase: they show no bands that are assignable to the phase T and are different from phase M bands (such as

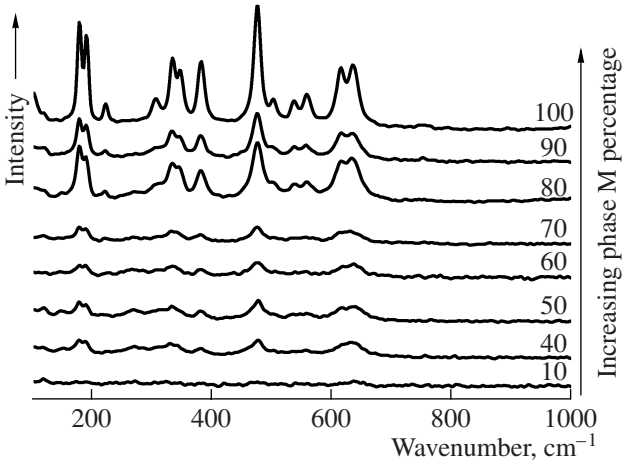

Fig. 7. Raman spectra of ZrO_2 prepared by precipitation (arranged in the order of increasing phase M percentages) for samples listed in Table 1.

160 and 260 cm^{-1}). As the amount of the phase M falls below 70%, the intensity of the spectra decreases markedly. This can be due to structure defects consistent with the IR spectra of the samples.

The bands best defined in the IR spectra of the samples rich in the phase T are 580, 510, 420, and 360 cm^{-1}, which are due to this phase [20, 44]. A tendency to a higher symmetry causes by increasing Ca cation content (Fig. 6b) is observed for the samples containing 5–10 mol % CaO. The appearance of extra absorption bands as shoulders (which are assigned to symmetric and asymmetric O–Zr–O vibrations [20]) is evidence of tetragonal distortions in the pseudocubic phase, which remain partially after the introduction of Ca cations.

The diffuse reflectance spectra are sensitive to the coordination environment of the zirconium cations. The absorption edge in these spectra shows a red shift as the symmetry and the CN of zirconium decrease, so DRS can be if use in structure analysis of the polymorphic modifications of ZrO_2 [20, 46]. The absorption edge position changes in the order C-ZrO_2 ~ T-ZrO_2 > M-ZrO_2 > $SrZrO_3$ as the CN of Zr^{4+} changes (8 > 7 > 6) [20]. Some of the specific features of the electronic spectra at low energies are usually attributed to defects (oxygen vacancies, Zr^{3+}, etc.) or trigonal oxygen [20, 47]. Typical diffuse reflectance spectra of zirconia samples differing in the percentage of the phase T are presented in Fig. 8a. Along with the strong absorption band ~40000 cm^{-1}, whose position depends on the polymorphic modification of ZrO_2, extra absorption at 31000 is observed. It intensity is the highest for the samples rich in the phase M and is the lowest for the samples with the highest phase T content. In the latter case the absorption edge shows a blue shift. The intensity of the ~31000 cm^{-1} band was taken to be a measure of the amount of the phase M and/or defects. Because of the large contribution from this band to the reflection intensity for the samples with a large S_{sp} value, we determined the intensity of this band relative to the total

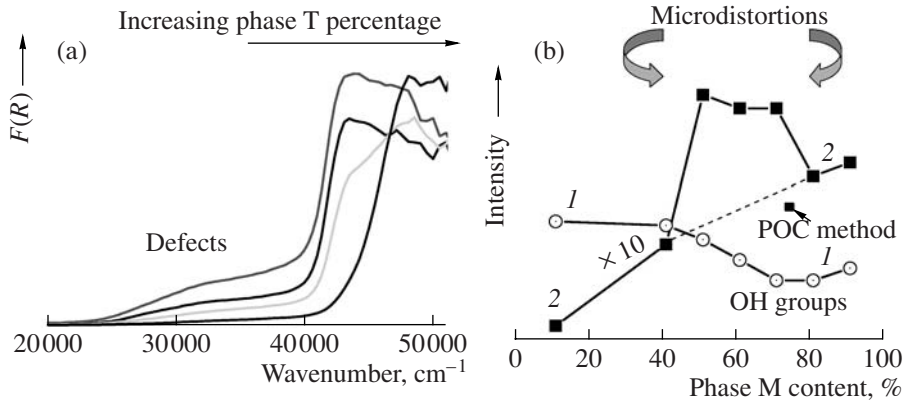

Fig. 8. (a) Diffuse reflectance spectra and (b) dependence of the (*1*) OH group concentration and (*2*) relative intensity of the defect band at 31000 cm^{-1} (I_{def}/I_{CTB})on the percentage of the phase M in ZrO_2 (500°C) for samples from Table 1.

absorption of the phases M and T at 48000–50000 cm^{-1}. A satisfactory correlation is observed between the intensity of the band at ~31000 cm^{-1} and the phase M content (Fig. 8b), except for the medium percentages. This growth of the band intensity can be attributed to defects/distortions in the phase M causes by the internal stresses between intergrown particles of the phases M and T (which is in agreement with IR and Raman spectroscopic data). The decreases in the total amount of bulk hydroxyls (as judged from the intensity of the absorption band at ~3400 cm^{-1} in the IR spectrum) would cause the formation of anionic vacancies and the transformation of the phase T into the phase M (Fig. 8b, curve *2*), but, because the formation of a reduced zirconium cation is unlikely under these conditions, the fluorite structure turns into a baddeleyite structure with polyhedra sharing not only corners, but also edges. The faults in the stacking of the anionic layers (Fig. 9a) due to the synthesis conditions or random factors even at the solution stage can cause microdistortions because of the structural mismatch between the anionic networks of the two different structure types. In the phase T-rich samples prepared by high-temperature precipitate ageing, the hydroxyls are bonded more strongly and are irremovable at 500°C.

Thus, the band at ~31000 cm^{-1} in the diffuse reflectance spectrum of ZrO_2 can be assigned to trigonal oxygen in the phase M, which results from the elimination of hydroxyls and from the partial conversion of the phase T into the phase M, and to the internal stresses that develop between intergrown particles of the phases M and T because of the structural mismatch.

As the Ca cation content is raised, the absorption edge in the diffuse reflectance spectrum shifts to higher energies. Extra absorption is observed at 34000–36000 cm^{-1}, and its relative intensity passes through a maximum at 2.4 mol % CaO and falls off at higher promoter contents (Fig. 10, curve *1*). The quantity of residual hydroxyls also decreases with increasing promoter content (Fig. 10, curve *2*). In this case, this absorption should be assigned not to oxygen vacancies, but to structure distortions, whose effect weakens as the promoter content is raised. The calcium cations in ZOC solutions, located between tetramers, prevent the formation of ribbonlike/sheetlike structures and thereby direct tetramer linking towards the formation of the phase T precursor (rodlike structures). In the oxide lattice, these cations likely occupy positions between ZrO_2 crystallites without generating oxygen vacancies. Interacting with terminal hydroxyls of the tetramer, the Ca cations reduce the number of free hydroxyls to an extent proportional to the percentage of the promoter in the sample, and this is the cause of the well-known thermal stability of doped ZrO_2. In pure ZrO_2, the terminal hydroxyls are bonded less strongly and are removed by calcination, giving rise to a T-to-M phase transition and crystallite sintering. In particles formed from different complexes (different precursors of the phases T and M) in solution, microdistortions due to the structural mismatch between the phases appear along their intergrowth boundaries. It is essential for the synthesis of the metastable phases T and C that the local coordination environment of the zirconium cation in the starting salt (oxynitrate or oxychloride) change from the square antiprism to a fluorite-like polyhedron. This change requires energy, because it is necessary that half of the oxygen atoms be shifted from the middle points of the edges to the corners of the cube. This process can be carried out efficiently by prolonged ageing of the precipitate at an elevated temperature. Because of the larger proportion of ribbonlike association species in the presence of Sr cations, the layered perovskite structure is detectable at lower Sr concentrations [10]. The breaking of Zr–Zr bonds in the tetramer in aqueous solution can take place only upon the introduction of a strong complexing agent [48]. In the presence of phosphate ions, this causes the formation of framework structures with a large surface area [49].

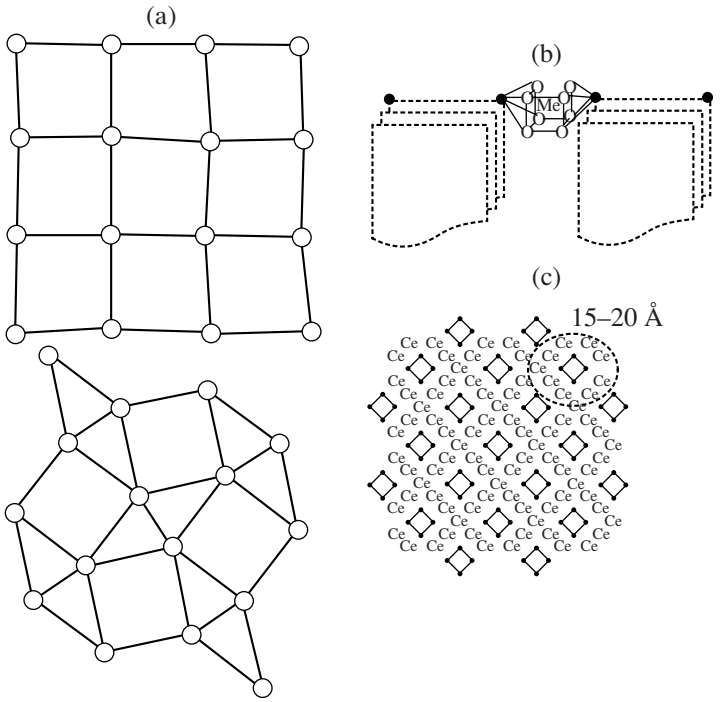

Fig. 9. (a) Two types of baddeleyite anionic networks, (b) models of the phases T and C of ZrO_2 containing minor amounts of a promoter, and (c) the motif of the cationic sublattice of the most homogeneous fluorite $Ce_{0.5}Zr_{0.5}O_2$.

ZIRCONIUM-CONTAINING MIXED OXIDES WITH A FLUORITE STRUCTURE

There have been many studies devoted to the preparation of Ce–Zr–O catalysts, their characterization, and their properties in oxidation processes [1, 35, 50–57]. These studies have been focused on enhancing or conserving the oxygen buffering capacity (OBC) and thermal stability of mixed oxides in connection with the problem of automotive exhaust neutralization. The increased OBC of Ce–Zr–O solid solutions or compounds is usually attributed to distortions in the fluorite structure (Fig. 1a) caused by the replacement of Ce^{4+} cations by Zr^{4+} cations, which have a smaller ionic radius. This was reported to generate an interstitial oxygen–anionic vacancy pair and extra anionic vacancies (Ce^{3+} cations) [58], but the cause of the formation of the reduced cations and their number have not been discussed. There has been no experimental evidence of distortions taking place in the local environment of cerium cations. Moreover, the higher OBC of Ce–Zr–O solid solutions was attributed to distortions in the coordination environment of zirconium cations or to a decrease in the strength of Zr–O bonds in the laminar structure [59, 60], although the reduction of zirconium cations has been detected only under severe conditions above 800°C. There is no consensus as to the composition range in which the OBC is the highest and as to how OBC depends on whether the material is single-phase or heterogeneous [14, 58–66]. The defect structure of Ce–Zr–O materials and its dependence on the synthetic method are poorly understood issues. In particular, this is true for the properties of these materials at the solution-and-precipitate stage of the synthesis.

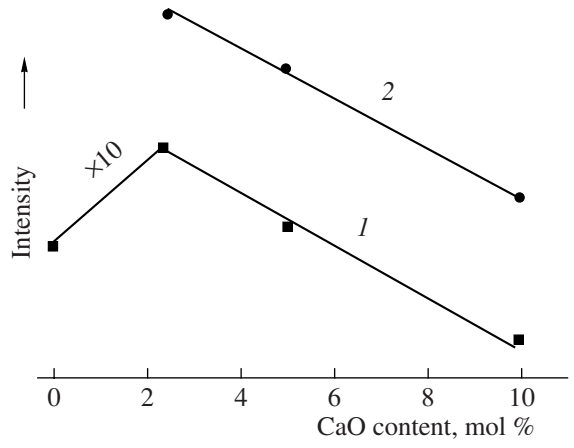

Fig. 10. (*1*) Relative intensity of the DRS band at 34000–36000 cm^{-1} and (*2*) the total concentration of bulk hydroxyls (according to IR spectroscopic data) as a function of CaO concentration in ZrO_2.

Dependence of the Defect Structure of the Fluorite-Like Ce–Zr–O Solid Solution on the POC Synthesis Conditions

According to the phase diagram of the ternary system Ce–Zr–O, a number of phases can form in this system below 1000°C, depending on the component con-

centrations [1]. At cerium contents below 10 mol %, the dominant phase is the phase M of ZrO_2. At high cerium contents of >80 mol %, a CeO_2-based fluorite phase is observed. A number of metastable tetragonal phases can form in the intermediate region. The boundaries between these phases are a matter of convention to a considerable extent, particularly near the equimolar composition and in the cerium-rich region, because all of these phases have the same fluorite-type cationic sublattice in which the oxygen atoms are displaced from their regular positions. This is manifested as extra bands in the Raman spectrum. As the lattice symmetry decreases, the optical mode F_{2g} from the fluorite structure in the Raman spectrum (465 cm^{-1}) splits into six active modes ($A_{1g} + 3E_g + 2B_{1g}$), which are characteristic of the phase T [67]. The situation is less clear for nanodisperse materials, because the Raman intensity falls dramatically as the surface is disordered.

According to Vegard's rule, in the Ce–Zr–O system, the replacement of Ce^{4+} cations (ionic radius of 0.97 Å) by Zr^{4+} cations with a smaller ionic radius (0.84 Å) must cause a decrease in the unit cell parameter (unit cell contraction). For example, the unit cell parameter decreases from 5.411 to 5.270 ± 0.010 Å as the cerium content decreases from 100 to 50 mol % [1]. For nanodisperse samples, the decrease in the unit cell parameter depends on the synthesis method and can be much smaller (Fig. 11). On the one hand, an obligatory quality criterion for mixed oxide preparation methods is the homogeneity of the distribution of the components. On the other hand, for Ce–Zr–O solid solutions, another possible criterion is the unit cell parameter, which must decrease in proportion to the percentage of zirconium cations, whose ionic radius is smaller. As was demonstrated above, the kind of the starting zirconium salt (oxychloride or oxynitrate) or, more exactly, the structure of the polyhydroxo complexes in the solution can have an effect on the completeness of the interaction between the components in the synthesis of mixed oxides. At the same time, Ce^{3+} cations, which have a larger ionic radius and can be stabilized in the synthesis of ultrafine powders and in the case of incomplete precursor oxidation, can increase the unit cell parameter of the solid solution.

Making use of the effect of POC synthesis parameters (crystalline hydrate of a salt or solution, ratio between the metal cations and the chelating agent) on the phase composition of Ce- and Zr-containing catalysts, we were able to determine the conditions affording an ultrafine product with a sufficiently homogeneous component distribution, as is evident from the unit cell parameter data for the fluorite-like solid solution in a wide composition range (Fig. 11, curve *2*) [2]. The hydroxyl concentration in this solid solution is higher than is observed in pure CeO_2 (Fig. 11, curve *3*). The Ce^{3+} concentration in the solid solution calcined at 700°C is no higher than 1%. Figures 12 and 13 illustrate the effect of the degree of homogeneity of solid solutions of different compositions on the size and

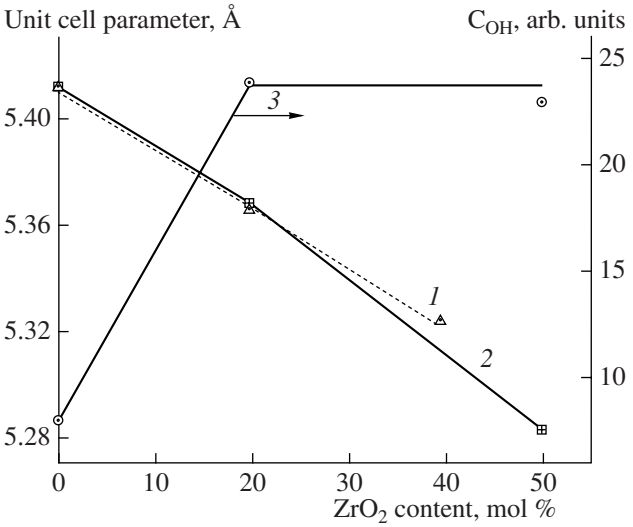

Fig. 11. (*1*, *2*) Unit cell parameter of the fluorite-like Ce–Zr–O solid solution as a function of the ZrO_2 content for samples prepared by (*1*) coprecipitation using a Ce^{4+} salt and ZON [1] and (*2*) the POC method using cerium(III) nitrate and ZOC [2]. (*3*) Concentration of residual OH groups (IR absorption band at 3500 cm^{-1}) in samples synthesized by the POC method.

intensity of extended defects and on distortions in the local environment of the cerium cations. For $Ce_{0.8}Zr_{0.2}$, as the degree of homogeneity increases, the intensity of the defects pertaining to the nonstoichiometric oxides Ce_nO_m decreases because of the changes in the structure of interdomain boundaries and the diluting effect of zirconium. The red shift of the defect band and the blue shift of the charge transfer band (CTB) are evidence that there are marked distortions in the environment of the cerium cations. This fact is partially due to the formation of a short Ce–O bond upon the replacement of an oxygen atom to, e.g., an interstitial site. For the equimolar composition, the defect size is reduced to 10–25 Å and the defect intensity increases substantially with an increasing degree of homogeneity (Fig. 13). This is accompanied by strengthening of distortions around the cerium cations. As a result, the low-frequency edge of the CTB is redshifted, the band itself is closer to the defect band, and there is a large amount of weakly bonded oxygen. The unit cell parameter *a* for this composition is 5.280 Å, which is in satisfactory agreement with its theoretical value of 5.260–5.270 Å and with the *a* values that were observed for the solid solutions obtained using more complicated synthesis methods and more expensive starting compounds. Thus, the defect structure is governed by the degree of homogeneity of the solid solution. Under optimal conditions, when ZOC solutions are used, the formation of chelates with an appropriate stoichiometry (metal : citric acid = 1 : 6–10) [2] makes it possible to hamper tetramer condensation substantially and to obtain fine-

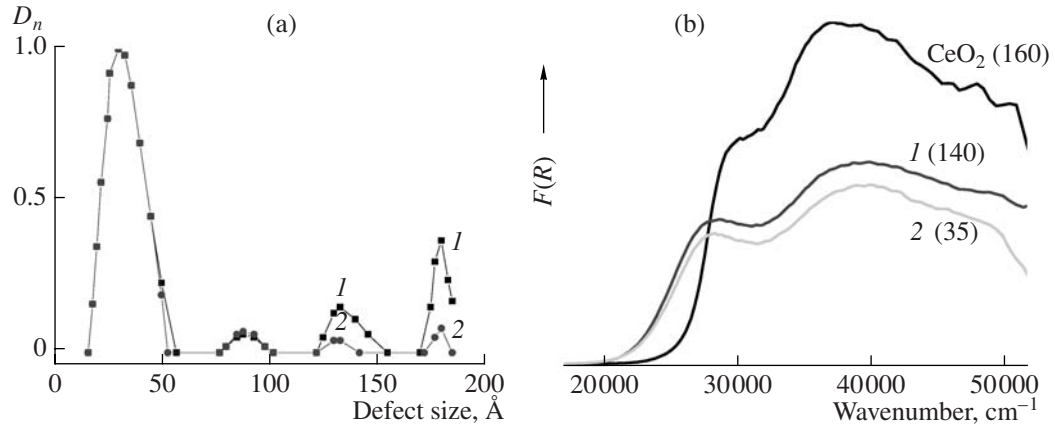

Fig. 12. (a) Defect size distribution (SAXS data) and (b) diffuse reflectance spectrum for $Ce_{0.8}Zr_{0.2}$ prepared by the POC method under different conditions. The unit cell parameter is a = (*1*) 5.380 and (*2*) 5.368 Å [2]. The parenthesized numbers in Fig. 12b are the relative intensities of the defects identified by SAXS, including for CeO_2.

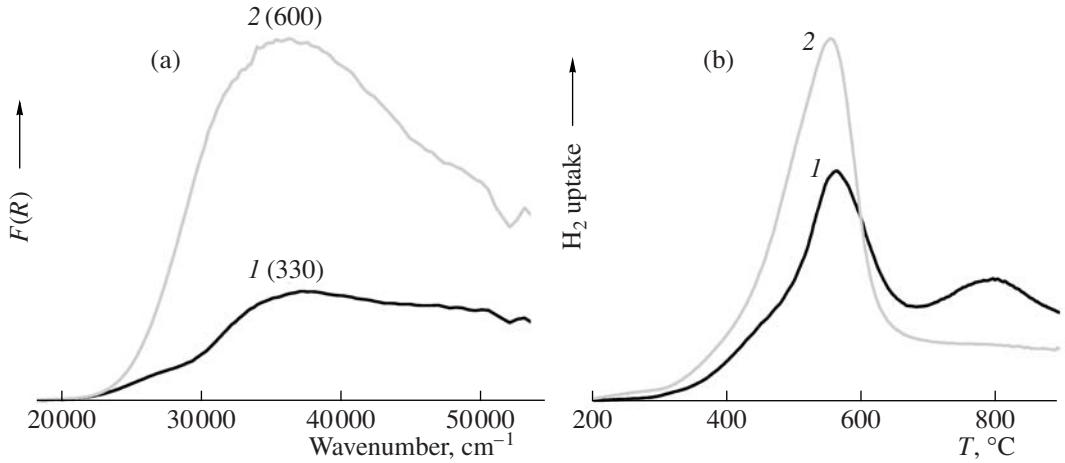

Fig. 13. (a) Diffuse reflectance and (b) H_2 TPR spectra of $Ce_{0.5}Zr_{0.5}$ prepared by the POC method under different conditions. The unit cell parameter is a = (*1*) 5.385 and (*2*) 5.280 Å [2]. The parenthesized numbers in Fig. 13a are the relative intensities of the defects identified by SAXS, whose dominant size is 10–25 Å.

particle mixed oxides with a sufficiently homogeneous component distribution.

Dependence of the Defect (Real) Structure of the Solid Solution $Ce_{0.5}Zr_{0.5}$ on the Synthesis Method

Examination of nuclei of equimolar phases prepared by coprecipitation (with precipitate ageing at 90°C for 0–22 h) and by the POC method (at various polymerization stages) from aqueous solutions of cerium nitrate and ZOC or zirconium acetate (ZAc) (which had similar particle size distributions (Fig. 4a)) demonstrated that significant Ce^{3+} oxidation in the mixed hydroxide precipitate at 90°C occurs after 10-h-long ageing, as is indicated by the precipitate turning yellow. After 22 h, the unit cell parameter of the solid solution is a = 5.326 Å (coherent-scattering domain size of 20 Å), which is somewhat larger than a for the samples calcined 300–500°C (5.289 Å). The increased value of a may be due to the residual Ce^{3+} cations and hydroxyls. The Raman spectrum of the precipitate is similar to the spectrum of the calcined sample with tetragonal distortions, but it has a much lower intensity because of the heavily disordered anionic sublattice. It shows extra bands at 780 and 1040 cm^{-1}, which are assignable to vibrations of low-coordinated, octahedral Zr/Ce cations (as in $BaZrO_3$ [68]) and to bending vibrations of the Zr–O–H fragment [69], respectively. The ageing of the precipitate includes both the oxidation of cerium cations and changes in their local environment. EXAFS data for the local structure of aged precipitates (Zr–Zr and Zr–O distances) are in close agreement with the structure parameters of the tetramers and with those of nanoparticles in pillared clay [6, 7]. This suggests that

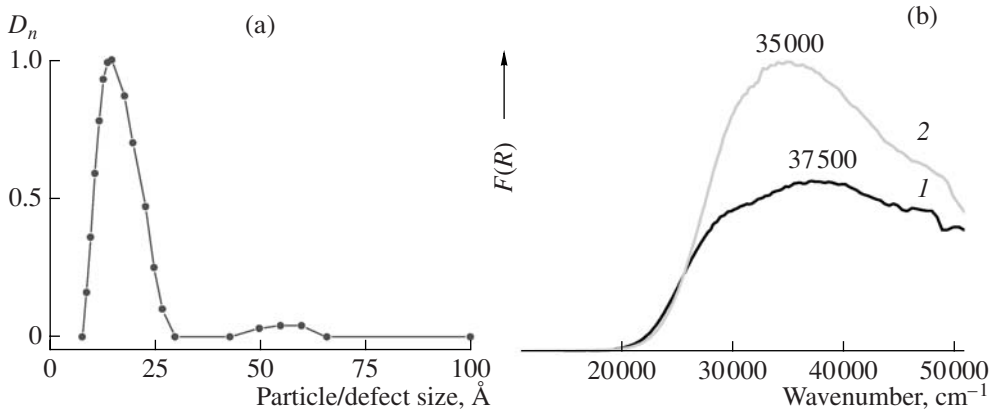

Fig. 14. (a) Size distribution of extended defects (SAXS data) in aged $Ce_{0.5}Zr_{0.5}$ hydroxide (coprecipitation method), in the polymer (POC method), and in the sample calcined at 700°C. (b) Diffuse reflectance spectrum of the $Ce_{0.5}Zr_{0.5}$ sample prepared by (*1*) coprecipitation and (*2*) the POC method. T_{calcin} = 700°C.

the solid solution has a higher degree of dispersion than crystalline fluorite [3, 4]. For the Zr–Ce sphere, the averaged Ce–Ce distance (≈3.4 Å, CN = 0.5–0.7) is radically different from the same distance in CeO_2 (Ce–Ce ≈ 3.7–3.8 Å, CN = 8.0–8.5) [3, 4].

Nearly the same defect size distribution is observed for the phase nuclei forming during the coprecipitation and POC procedures (Fig. 14a), which is similar to the distribution characterizing formed mixed oxides calcined at 700°C. The position of the main peak, 18 Å, indicates the region of an increased electron density due to the defects located around Zr_4 oxide clusters (or around tetramers in the solution) surrounded by cerium cations. This value is fairly consistent with the size of the Zr_4 oxide cluster formed from the tetramer (~10 Å) and with the double Ce–O distance (2.4 × 2 ~ 5 Å).

Thus, the structure of the nuclei of the fluorite phase of the mixed oxide is based on the Zr_4 oxide cluster/tetramer, which is bonded with cerium cations through the oxygen atoms of terminal hydroxyls. The basic changes taking place in the course of ageing are the ultimate oxidation of cerium cations, an increase of CN to 8, and the change of the coordination environment of the zirconium cations from a square antiprism to a fluorite-like polyhedron.

The unit cell parameter of the calcined samples prepared by coprecipitation is 5.304 and 5.294 Å for ZAc and ZOC, respectively, and is somewhat different from that of the sample prepared by the POC method (a = 5.280 Å). The increased a value is due not to the presence of Ce^{3+} cations, since their amount is as small as ~0.6 wt %, but to the presence of unbound ZrO_2 undetectable by X-ray diffraction (which was, however, detected by FTIR spectroscopy; Fig. 15a). Although the defect sizes in the samples prepared by coprecipitation and POC method are similar, the distortions in the local environment of the zirconium cations are better defined in the POC sample (Fig. 14b).

Thus, fine-particle solid solution phases with similar unit cell parameters result from the two synthetic procedures. The POC method yields a more defective material owing to the more homogeneous component distribution. In part, this is also due to the fact that, in this method, the oxidation of cerium cations to Ce^{4+} in the mixed oxide takes place at a higher temperature (~300°C) upon the burnout of the organics and the carbon component. For increasing the OBC of the Ce–Zr–O phase, the samples prepared by conventional methods should be kept under reductive conditions (1100°C) and then reoxidized at a lower temperature (500°C) [59, 63, 65]. Because of the low mobility of the cations, the low-temperature reoxidation of the reduced mixed oxide likely yields a defect structure similar to the structure initially resulting from the POC synthesis. Note that, although there have been numerous studies of Ce–Zr–O fluorites, TEM data have not revealed any distinctions between the defect structures of the samples examined.

The higher degree of imperfection/disorder of the Ce–Zr–O solid solution prepared by the POC method as compared to the sample prepared by coprecipitation is also evident from FTIR spectroscopic data. It manifests itself as a higher concentration of surface hydroxyls (absorption bands at 3680 and 3665 cm^{-1}) and hydrogen-bonded bulk hydroxyls (3200–3500 cm^{-1}) [3] (Fig. 15a). Free hydroxyls actually do not characterize the real surface composition. They are species remaining after the partial dehydroxylation of the sample during its conditioning in vacuo before recording a spectrum. Therefore, the quantity of surface hydroxyls characterizes the strength of their bonds with cations. The much lower intensity of the absorption bands from free hydroxyls for the samples prepared by coprecipitation is evidence that these hydroxyls are weakly bonded to the cations. The band at 3790 cm^{-1}, which is assigned

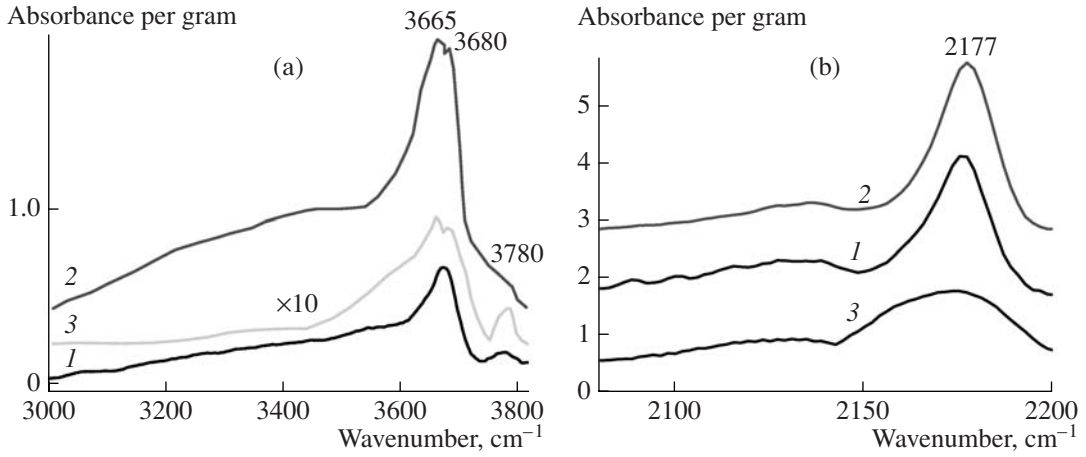

Fig. 15. FTIR spectra of (a) $Ce_{0.5}Zr_{0.5}$ calcined at 700°C in the region of hydroxyl vibrations and (b) adsorbed CO: (*1*) POC method, a = 5.385 Å; (*2*) POC method, a = 5.280 Å; (*3*) coprecipitation method, a = 5.304 Å. The amount of adsorbed CO is (*1*, *2*) 16 μmol and (*3*) 10 Torr.

to vibrations of the terminal OH groups in partially stabilized ZrO_2 [70], is due to the presence of ultrafine free ZrO_2 undetectable by X-ray diffraction. The formation of bound bulk hydroxyls in the POC method (absorption band at 3500 cm^{-1}) is possible at domain sintering boundaries (e.g., through domain superimposition, as is clear from TEM images [3]), and this is favorable for a higher thermal stability of the solid solution. In the region of the vibrations of surface carbonyls bonded with coordinatively unsaturated sites (isolated Ce^{4+} or Zr^{4+} cations), the absorption band at 2180 cm^{-1} [3] for the sample prepared by coprecipitation remains weak even after the adsorption of 10 Torr of CO (Fig. 15b), indicating that the surface concentration of these carbonyl groups in the coprecipitated sample is lower than is observed in the POC sample. The specific features of the defect structure of the surface have an effect on the state of platinum supported by impregnation. Supported platinum is stabilized as oxide cations (2180 cm^{-1}), mixed metal oxide clusters (2130 cm^{-1}), and metal clusters 20–40 Å in size (2040–2070 cm^{-1} [3]), as is demonstrated in Fig. 16. The higher degree of imperfection of the most homogeneous fluorite favors the stabilization of mixed platinum clusters in surface layers in the vicinity of extended defects (as is indicated by the SAXS signal being weaker after the supporting of platinum [3]), which are masked by adsorbed CO, but make lattice oxygen highly mobile [3].

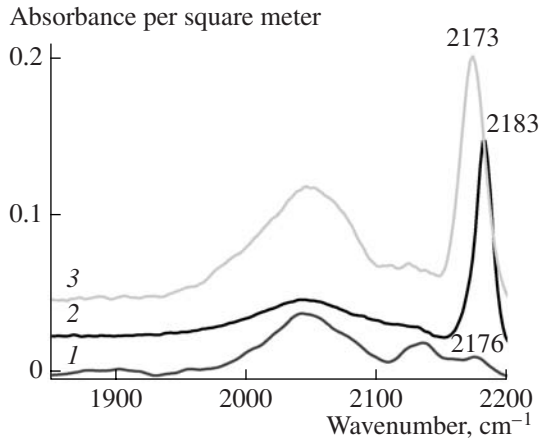

Fig. 16. Influence of the synthesis method and the homogeneity of the $Ce_{0.5}Zr_{0.5}$ fluorite on the state of the surface platinum sites (1.4 wt % Pt) according to FTIR data for adsorbed CO in the surface carbonyl vibration region at a CO adsorption of 16 μmol: (*1*) POC method (a = 5.385 Å), (*2*) POC method (a = 5.280 Å), and (*3*) coprecipitation method (a = 5.304 Å).

Effects of the Radius and Oxidation State of Cations on the Microstructure and Defectiveness of the Ce–Me–(Zr)–O Solid Solution

The introduction of lower valence ions in CeO_2 generates two types of defects: pure anionic vacancies form upon the introduction of MeO, and trimers containing two cerium cations and an anionic vacancy result from doping with Me_2O_3 [1]. The stability of a defect cluster in which a vacancy is located near a doping cation depends on the radius of the cation. A significant effect on the bond energy is exerted by the relaxations due to the introduction of a promoter: small cations reduce the CN, and large cations (including Ce^{3+}) shift away from the cluster defect of the promoter without breaking any bonds. This changes the Ce–O and Ce–Ce bond lengths.

The formation of a statistical solid solution implies, first of all, a homogeneous distribution of the introduced component in the host matrix. The solubility limit of a cation with an ionic radius larger than that of Ce^{4+} in CeO_2 typically does not exceed 20–30 mol % [1, 3, 8, 11–13, 71]. At higher cation concentrations, the

effect of the structural features of the promoter itself strengthens. Lanthanide cations have large ionic radii, and their stable oxidation state is +3, except for the praseodymium ion, which is stable in the oxidation states +3 and +4. In passing from praseodymium to gadolinium, samarium, neodymium, and lanthanum, the ionic radius of the cation increases from 1.03 to 1.18 Å. While cerium shows a strong tendency to CN = 8, these cations can have a larger CN. The cations with an ionic radius below 1.0 Å tend to nave a smaller CN. For transition metal cations with an ionic radius of ~0.6 Å, the most stable oxygen coordination polyhedra are an octahedron and a tetrahedron.

An analysis of the literature [71–74] demonstrates that, in the introduction of lanthanide cations into the CeO_2 fluorite structure, the unit cell parameter changes in proportion to the amount of promoter introduced, irrespective of the heat-treatment temperature (500–1500°C) and the synthesis method (provided that the synthesis method ensures a uniform distribution of the components). At a fixed promoter concentration, the larger the cation radius, the larger the unit cell parameter (Fig. 17). Upon the introduction of zirconium, the unit cell parameter decreases because the zirconium ion has a smaller radius. For small cations (such as copper, manganese, and aluminum), it remains unchanged even at very high promoter concentrations [75, 76]. For example, in CeO_2 + 50–75 mol % Al_2O_3 synthesized by the POC method, even after calcination at 700°C, X-ray diffraction reveals only a fluorite phase with an invariable unit cell parameter, while aluminum oxide is present as a finely divided phase. The coherent-scattering domain size for CeO_2 is 20–25 Å, and S_{sp} = 116–185 Å. The small cations are "diluents" with respect to CeO_2. The introduction of large cations of a lanthanide or zirconium into CeO_2 diminishes the coherent-scattering domain size from 500 to 70–150 Å for the samples calcined at 500–700°C [3]. Therefore, the uniform distribution of the dopant cations, which is indicated by the changes in the unit cell parameter (X-ray diffraction data), may be accompanied by the formation of interdomain boundaries within the fluorite structure that have different properties and prevent the formation of larger particles. This is consistent with the familiar concept that the fluorite structure is an open system capable of tolerating high degrees of disorder. At the same time, this indicates that fluorite is the structure-forming system favoring a decrease in the particle size [3, 4].

The introduction of Sm or La cations reduces the particle size (resulting in a coherent-scattering domain size of 70–150 Å) and diminishes the size of extended defects to 10–25 Å [3]. An extended defect is a module based on the nonstoichiometric oxide Me_nO_m (Me = Ce^{3+}, Sm^{3+}, La^{3+}) that can be located not only at an interdomain boundary, as in the case of CeO_2, but, most likely, within a fluorite particle. An analysis of the distortions in the fluorite structure caused by the introduction of Sm, La, and Zr cations demonstrates that the larger the radius of the cation, the greater these distortions, and this is confirmed by DRS data and by the decrease in the Raman intensity at a fixed promoter content because of the disordering of the anionic sublattice (Fig. 18). The introduction of Sm shifts the fluorite band from 463 to 457 cm^{-1}, and the introduction of the same amount of Zr shifts this band to 472 cm^{-1}, indicating a weakening and strengthening of the Me–O bond, respectively. This results in a larger fraction of weakly bonded oxygen for Sm and La (according to H_2 TPR data). The increase in the degree of disorder and distortion taking place as the Zr (not Sm) concentration is raised to 50 mol % allows this concentration to be increased further (Figs. 18b, 18c). EXAFS spectroscopy is less sensitive to the fine defect structure: it indicates the existence of two averaged Ce–O distances not only in CeO_2, but also in Ce–Sm–O and Ce–Zr–O samples [2, 3]. According to secondary ion mass spectrometry (SIMS) data, an increase in the relative promoter concentration in the surface layers is observed upon the introduction of Sm (5–40 mol %) or Zr (50 mol %) into CeO_2 [3]. These changes can be due to the variation of the composition and density of extended $Ce(Sm)_nO_m$ defects within the fluorite structure and to the existence of structural modules with a locally increased cation concentration in the Zr_4 oxide cluster.

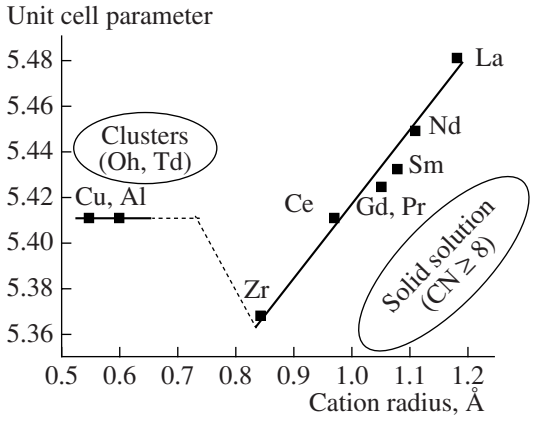

Fig. 17. Unit cell parameter of the fluorite phase as a function of the promoter cation radius (for the lanthanides, the degree of substitution is 20 mol %).

Thus, the chemical nature of the promoter has an effect on the fluorite microstructures and on the Ce–O bond strength. The weakening of the Ce–O bonds both at interdomain boundaries and in the bulk facilitates the reduction of surface oxygen (peak at 400–500°C) and bulk oxygen (600–900°C), particularly in the lanthanum- and samarium-modified samples (Fig. 18b). For zirconium cations, as compared to Sm (La) cations, bulk reduction begins at a higher temperature. The fraction of reduced surface oxygen in this case is somewhat larger, but the corresponding peak is shifted to 500–600°C. Estimation of the total amount of oxygen removed from mixed oxide samples per gram of CeO_2 in an H_2 TPR run (20–900°C) demonstrated that, irre-

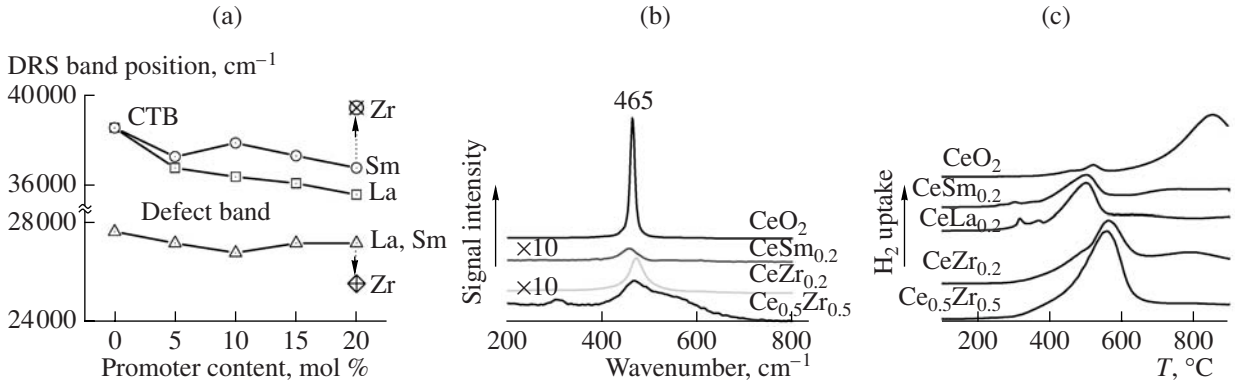

Fig. 18. Effect of cerium cation distortions in Ce–Me–O fluorites (Me = Sm, La, Zr) identifiable by (a) DRS (CTB and defect band) and (b) Raman spectroscopy on the Ce–O bond strength estimated from (c) H_2 TPR data.

spective of the Me^{3+} promoter concentration, this amount is similar to the amount characteristic of the pure dioxide [3]. The amount of removed oxygen is somewhat larger for La than for Sm because of the more pronounced weakening of the Ce–O bonds in the latter. A much larger amount of oxygen is removable from Zr-modified ceria. Thus, the anionic vacancies resulting from the doping of CeO_2 with cations in a lower oxidation state cause a much greater disordering of the anionic sublattice, facilitating oxygen removal, but do not increase the total amount of removable oxygen. The microstructure and composition of the domain sintering boundaries have a strong influence on oxygen removal from modified binary fluorite.

The effects of the nature and ionic radius of the promoter in more complex oxides (Ce–Zr–Me–O) are determined by the Ce/Zr ratio and have some specific features for cerium-rich compositions (up to the equimolar composition), as well as for zirconium-rich compositions [4]. Cations with a small ionic radius form oxide clusters around Ce–Zr–O nanodomains, and the large cations of lanthanides mainly replace cerium cations in the structural module (Fig. 9c) and/or stabilize the metastable phases T and C. For example La (Y) cations introduced into zirconium-rich Ce–Zr–O compositions in the synthesis by coprecipitation enhance the thermal stability of these compositions [77–79] according to the model presented in Fig. 9b.

Identification of Interstitial Oxygen in the Ce-Containing Fluorite-Like Solid Solution

The energetically most favorable type of defect in fluorites is IO, whose formation is accompanied by the formation of a short Me–O bond. If there are distortions in the local environment of cerium and zirconium cations (defect band in DRS, two short and two long Ce–O and Zr–O bonds, EXAFS data) [3], IO formation in cerium-containing materials can be detected as an O_2^- signal (e.g., the 1126 cm^{-1} absorption band in the IR spectrum) [3]. In an earlier work [58], the appearance of O_2^- was attributed to the stabilization of molecular oxygen in vacant regular positions generated by the displacement of oxygen to interstices in the presence of Ce^{3+} cations. In the Ce–Sm–O and Ce–Zr–La–O systems (Fig. 19), the amount of IO in the surface layers is proportional to the concentration of isolated anionic vacancies generated by the lower valence promoter with a larger ionic radius (Sm^{3+}, La^{3+}, Ce^{3+}) at small perturbations in the fluorite structure (promoter contents of ≤10 mol %) [3]. In CeO_2 and in equimolar Ce–Zr–O fluorite prepared by the POC method, in spite of heavy distortions, no IO formation was detected, but the IO concentration is higher in the samples prepared by coprecipitation. It is likely that the presence of Ce^{3+} cations is not a necessary condition for IO formation, because, in all samples in these systems, the Ce^{3+} concentration is below 1%. This can be due to the nonadditive character of the structural features of extended defects and of their concentration in the Ce–Zr–O fluorites as a function of composition. For the Ce–Sm–O system, it was shown that the oxygen diffusion rate (rate of oxygen removal in helium at 900°C) is proportional to the surface IO concentration.

Effect of the Defect Structure on the State of the Supported Active Component and on Its Catalytic Properties

The defect structure of the nanomaterials examined determines the forms in which the supported active component is stabilized by the formation of clustered species (islands) around the defects. This has an influence on the catalytic properties of the materials in low- and medium-temperature reactions not involving the oxygen of the catalyst, as well as in high-temperature processes because of the dependence of the mobility of lattice oxygen on the state of the active component. The highest activity in limonene diepoxide conversion (T_r = 25°C, CH_2Cl_2 as the solvent) is exhibited by sulfated

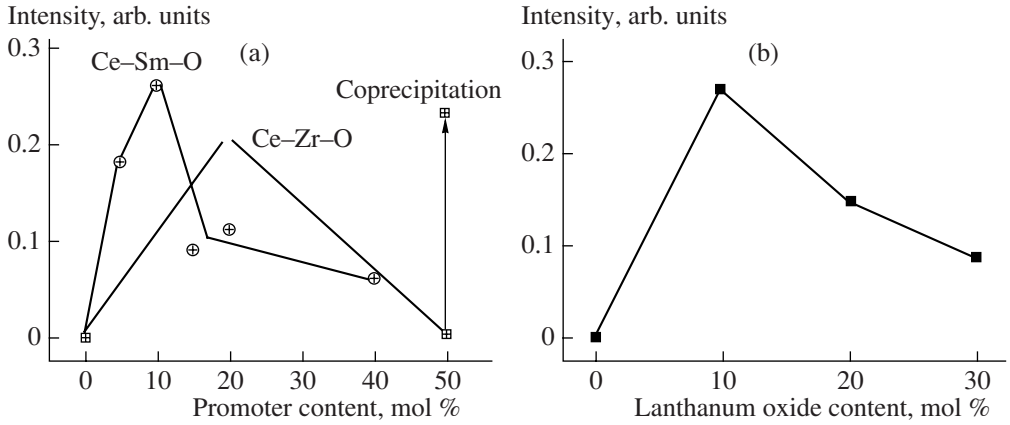

Fig. 19. Surface concentration of interstitial oxygen derived from the intensity of the 1126 cm^{-1} absorption band (O_2^-) on the amount of a promoter introduced into the fluorites (a) Ce–Sm(Zr)$_x$–O and (b) Ce–Zr–La$_x$–O. O_2 (100 Torr) was adsorbed onto the reduced surface.

ZrO_2, which is characterized by a high degree of imperfection (microdistortions) as compared to phases M and C [80]. As the extent of sulfation is increased, isolated sulfate ions (Lewis sites) turn into Brønsted-like clusters in spite of the large fraction of the free surface. This shows itself as changes in the selectivities with respect to limonene conversion products. The clusters of Pt (1.4 wt %) resulting from the supporting of platinum on the phase T of ZrO_2 are more active than the same clusters on the phase M or C in the water gas shift reaction (10% CO + 20% H_2O + 68% H_2) at 300°C owing to the higher concentration of nearest-neighbor hydroxyls, which are involved in this reaction. The higher activity of the platinum-containing Ce–Zr–O fluorites in this reaction is due to platinum metal clusters and anionic vacancies, which are mainly reoxidized by water molecules (coprecipitation method). It is not due to highly mobile lattice oxygen as in the case of samples prepared by the POC method [3]. The defect structure of fluorite, which depends on the preparation procedure, determines the state of supported platinum, which influences the methane activation rate, the reactivity of the surface, and the mobility of lattice oxygen [3, 11–13]. The ultrafine clusters of metallic platinum afford the highest rate of methane activation. The catalyst with the optimum oxygen mobility ensure highly efficient syngas synthesis by combining a high rate of partial methane oxidation with a high rates of methane steam and carbon dioxide reforming.

The higher NO_x SCR activity of the catalysts based on pillared clays (which contain discrete ZrO_2 nanopillars) compared to ultrafine bulk ZrO_2 [6, 39] is explained by the fact that these catalysts differ in terms of the structure of the surface clusters of the active component (CuO + Pt). Even supporting a small amount of copper (0.2 wt %) on ZrO_2 results in the stabilization of three-dimensional copper clusters on the surface [10]. At high percentages of supported metal, these clusters can be partially dispersed by special chemical treatment. At comparable concentrations copper on pillared clays is mainly stabilized as dimer oxide clusters. The more discrete form of the active component in the latter case (after subsequent supporting of 0.2 wt % Pt) optimizes the strength of nitrate/nitrite complex binding to the surface and the reactivity of hydrocarbons, reducing the contribution of nonselective combustion. This is the cause of the high low-temperature NO_x SCR activity of the catalysts based on pillared clays [5, 6, 8–10].

CONCLUSIONS

By widely varying the synthesis methods and conditions and characterizing the resulting fluorites by a variety of physicochemical methods, it was possible to construct models for the defect structure of CeO_2, ZrO_2, and related materials. The formation of the T- and C-modifications of ZrO_2 at medium calcination temperatures is due to their metastable structural organization, which is different from the structures of the known equilibrium phases. The phase composition of ZrO_2-based materials at the solution-and-precipitate stage is determined by the change of the local eight-atom environment of the zirconium cations in the tetramer from a square antiprism into a fluorite-like polyhedron through displacement of terminal oxygen anions and obeys the structure conformity principle in modification. The effects of the promoter radius and oxidation state on the structural features and defectiveness of cerium-containing fluorites of complex compositions were systematized. The distortions in the oxygen environment of the cerium cations are responsible for the presence of weakly bonded oxygen in these materials. The defect structure of the support/substrate determines the state of the supported active component and its catalytic properties. In the analysis of defect structure models of the nanomaterials, methods using low-energy radiation (SAXS, DRS, IR and Raman spectroscopy) are the

most informative, while X-ray diffraction allows only the structural type of the material and the coherent-scattering domain size (three-dimensional order of the cationic sublattice) to be determined.

ACKNOWLEDGMENTS

In this review, we used both literature data and results of studies supported by a number of Russian and foreign grants. We are grateful to all coworkers and authors of publications for their contribution to this work.

REFERENCES

1. *Catalysis by Ceria and Related Materials*, Catalytic Science Series, vol. 2, London: Imperial College Press, 2002.
2. Kuznetsova, T.G., Sadykov, V.A., Moroz, E.M., Trukhan, S.N., Paukshtis, E.A., Kolomiichuk, V.N., Burgina, E.B., Zaikovskii, V.I., Fedotov, M.A., Lunin, V.V., and Kemnitz, E., *Stud. Surf. Sci. Catal.*, 2002, vol. 143, p. 659.
3. Sadykov, V.A., Kuznetsova, T.G., Alikina, G.M., Frolova, Yu.V., Lukashevich, A.I., Potapova, Yu.V., Muzykantov, V.S., Rogov, V.A., Batuev, L.Ch., Kriventsov, V.V., Kochubei, D.I., Moroz, E.M., Zyuzin, D.A., Paukshtis, E.A., Burgina, E.B., Trukhan, S.N., Ivanov, V.P., Pinaeva, L.G., Ivanova, Yu.A., Kostrovskii, V.G., Neophytides, S., Kemnitz, E., and Scheurel, K., In: *New Topics in Catalysis Research*, N.Y.: Nova Publ., 2006, p. 97.
4. Kuznetsova, T., Sadykov, V., Batuev, L., Moroz, E., Burgina, E., Rogov, V., Kriventsov, V., and Kochubei, D., *J. Nat. Gas Chem.*, 2006, vol. 15, p. 149.
5. Sadykov, V.A., Kuznetsova, T.G., Bunina, R.V., Mezentseva, N.V., Efremov, D.K., Avdeev, V.I., Doronin, V.P., Kuznetsov, V.L., Volodin, A.M., Paukshtis, E.A., Alikina, G.M., Matyshak, V.A., and Lunin, V.V., *Mater. Res. Soc. Symp. Proc.*, 2005, vol. 876E, p. R8.21.1.
6. Sadykov, V.A., Kuznetsova, T.G., Doronin, V.P., Sorokina, T.P., Kochubei, D.I., Novgorodov, B.N., Kolomiichuk, V.N., Moroz, E.M., Zyuzin, D.A., Paukshtis, E.A., Fenelonov, V.B., Derevyankin, A.Ya., Beloshapkin, S.A., Matyshak, V.A., Konin, G.A., and Ross, J.R.H., *Mater. Res. Soc. Symp. Proc.*, 2002, vol. 703, p. 1.
7. Sadykov, V.A., Kuznetsova, T.G., Doronin, V.P., Sorokina, T.P., Alikina, G.M., Kochubei, D.I., Novgorodov, B.N., Paukshtis, E.A., Fenelonov, V.B., Zaikovskii, V.I., Rogov, V.A., Anufrienko, V.F., Vasenin, N.T., Matyshak, V.A., Konin, G.A., Rozovskii, A.Ya., Tretyakov, V.F., Burdeynaya, T.N., Ross, J.R.H., and Breen, J.P., *Chem. Sustainable Dev.*, 2003, vol. 11, p. 249.
8. Sadykov, V.A., Pavlova, S.N., Bunina, R.V., Alikina, G.M., Tikhov, S.F., Kuznetsova, T.G., Frolova, Yu.V., Lukashevich, A.I., Snegurenko, O.I., Sazonova, N.N., Kazantseva, E.V., Dyatlova, Yu.N., Usol'tsev, V.V., Zolotarskii, I.A., Bobrova, L.N., Kuz'min, V.A., Gogin, L.L., Vostrikov, Z.Yu., Potapova, Yu.V., Muzykantov, V.S., Paukshtis, E.A., Burgina, E.B., Rogov, V.A., Sobyanin, V.A., and Parmon, V.N., *Kinet. Katal.*, 2005, vol. 46, no. 2, p. 243 [*Kinet. Catal.* (Engl. Transl.), vol. 46, no. 3, p. 227].
9. Sadykov, V.A., Kuznetsova, T.G., Doronin, V.P., Moroz, E.M., Ziuzin, D.A., Kochubei, D.I., Novgorodov, B.N., Kolomiichuk, V.N., Alikina, G.M., Bunina, R.V., Paukshtis, E.A., Fenelonov, V.B., Lapina, O.B., Yudaev, I.V., Mezentseva, N.V., Volodin, A.M., Matyshak, V.A., Lunin, V.V., Rozovskii, A.Ya., Tretyakov, V.F., Burdeynaya, T.N., and Ross, J.R.H., *Top. Catal.*, 2005, vol. 32, p. 29.
10. Sadykov, V.A., Bunina, R.V., Alikina, G.M., Ivanova, A.S., Kochubei, D.I., Novgorodov, B.N., Paukshtis, E.A., Fenelonov, V.B., Zaikovskii, V.I., Kuznetsova, T.G., Beloshapkin, S.A., Kolomiichuk, V.N., Moroz, E.M., Matyshak, V.A., Konin, G.A., Rozovskii, A.Ya., Ross, J.R.H., and Breen, J.P., *J. Catal.*, 2001, vol. 200, p. 117.
11. Sadykov, V., Lunin, V., Kuznetsova, T., Alikina, G., Frolova, Yu., Lukashevich, A., Potapova, Yu., Muzykantov, V., Veniaminov, S., Rogov, V., Kriventsov, V., Kochubei, D., Moroz, E., Zuzin, D., Zaikovskii, V., Kolomiichuk, V., Paukshtis, E., Burgina, R., Zyryanov, V., Uvarov, N., Neophytides, S., and Kemnitz, E., M, *Stud. Surf. Sci. Catal.*, 2004, vol. 147, p. 241.
12. Sadykov, V.A., Kuznetsova, T.G., Alikina, G.M., Frolova, Y.V., Lukashevich, A.I., Potapova, Y.V., Muzykantov, V.S., Rogov, V.A., Kriventsov, V.V., Kochubei, D.I., Moroz, E.M., Zyuzin, D.I., Zaikovskii, V.I., Kolomiichuk, V.N., Paukshtis, E.A., Burgina, E.B., Zyryanov, V.V., Uvarov, N.F., Neophytides, S., and Kemnitz, E., *Catal. Today*, 2004, vols. 93–95, p. 45.
13. Sadykov, V.A., Kuznetsova, T.G., Frolova, Yu.V., Alikina, G.M., Lukashevich, A.I., Rogov, V.A., Muzykantov, V.S., Pinaeva, L.G., Sadovskaya, E.M., Ivanova, Yu.A., Paukshtis, E.A., Mezentseva, N.V., Batuev, L.Ch., Parmon, V.N., Neophytides, S., Kemnitz, E., Scheurell, K., Mirodatos, C., and van Veen, A.C., *Catal. Today*, 2006, vol. 117, p. 475.
14. Bulgakov, N.N., Sadykov, V.A., Lunin, V.V., and Kemnitz, E., *React. Kinet. Catal. Lett.*, 2002, vol. 76, no. 1, p. 103.
15. Aneggi, E., Llorca, J., Boaro, M., and Trovarelli, A., *J. Catal.*, 2005, vol. 234, p. 88.
16. Terribile, D., Trovarelli, A., Llorca, J., Leitenburg, C., and Dolcetti, G., *J. Catal.*, 1998, vol. 178, p. 299.
17. Tsunekawa, S., Sahara, R., Kawazoe, Y., and Ishikawa, K., *Appl. Surf. Sci.,* 1999, vol. 152, p. 53.
18. Nagai, Y., Yamamoto, T., Tanaka, T., Yoshida, S., Nonaka, T., Okamoto, T., Suda, A., and Sugiura, M., *Catal. Today*, 2002, vol. 74, p. 225.
19. Mochizuki, S., *Phys. Status Solidi B*, 1982, vol. 114, no. 1, p. 189.
20. López, E.F., Escribano, V.S., Panizza, M., Carnasciali, M.M., and Busca, G., *J. Mater. Chem.*, 2001, vol. 11, p. 1891.
21. Rao, G.R. and Mishra, B.G., *React. Kinet. Catal. Lett.*, 2002, vol. 75, p. 251.
22. Garcia, T., Solsona, B., and Taylor, S., *Catal. Lett.*, 2005, vol. 105, p. 183.
23. Benfer, S. and Knozinger, E., *J. Mater. Chem.*, 1999, vol. 9, p. 1203.

24. Afanasiev, P., Thiollier, A., Breysse, M., and Dubois, J.L., *Top. Catal.*, 1999, vol. 8, p. 147.
25. Jung, K.T. and Bell, A.T., *J. Mol. Catal. A: Chem.*, 2000, vol. 163, p. 27.
26. Chuah, G.K., Jaenicke, S., Cheong, S.A., and Chan, K.S., *Appl. Catal., A*, 1996, vol. 145, p. 267.
27. Mercera, P.D.L., Van Ommen, J.G., Doesburg, E.B.M., Burggraaf, A.J., and Ross, J.R.H., *Appl. Catal.*, 1990, vol. 57, p. 127.
28. Chuah, G.K., Liu, S.H., Jaenicke, S., and Li, J., *Microporous Mesoporous Mater.*, 2000, vol. 39, p. 381.
29. Garvie, R.C., *J. Phys. Chem.*, 1978, vol. 82, no. 2, p. 218.
30. Petrunin, V.F., Popov, V.V., Hunzhi, Zh., and Timofeev, A.A., *Neorg. Mater.*, 2004, vol. 40, p. 251 [*Inorg. Mater.* (Engl. Trans.), vol. 40, p. 251].
31. Stefanic, G., Music, S., Grzeta, B., Popovic, S., and Sekulic, A., *J. Phys. Chem. Solids*, 1998, vol. 59, nos. 6–7, p. 879.
32. Wang, J.A., Valenzuela, M.A., Salmones, J., Vazquez, A., Garcia-Ruiz, A., and Bokhimi, X., *Catal. Today*, 2001, vol. 68, p. 21.
33. Fabris, S., Paxton, A.T., and Finnis, M.W., *Acta Mater.*, 2002, vol. 50, no. 20, p. 5171.
34. Polezhaev, Yu.M., Afonin, Yu.D., and Zhilyaev, V.A., *Izv. Akad. Nauk SSSR, Neorg. Mater.*, 1977, vol. 13, no. 3, p. 476.
35. Ivanova, A.S., *Kinet. Katal.*, 2001, vol. 42, no. 3, p. 394 [*Kinet. Catal.* (Engl. Transl.), vol. 42, no. 3, p. 354].
36. Loong, C.-K., Richardson, J.W., and Ozawa, M., *J. Catal.*, 1995, vol. 157, p. 636.
37. Kim, D.-J., *J. Am. Ceram. Soc.*, 1989, vol. 72, no. 8, p. 1415.
38. Benard, P., Louer, M., and Louer, D., *J. Solid State Chem.*, 1991, vol. 94, no. 1, p. 27.
39. Toth, L.M., Lin, J.S., and Felker, L.K., *J. Phys. Chem.*, 1991, vol. 95, p. 3106.
40. Clearfield, A. and Vaughan, P.A., *Acta Crystallogr.*, 1956, vol. 9, p. 555.
41. Aberg, M., *Acta Chem. Scand., Ser. B*, 1977, vol. 31, p. 171.
42. Ohtaki, H., *Chem. Rev.*, 1993, vol. 93, p. 1157.
43. Efremov, D., Kuznetsova, T., Doronin, V., and Sadykov, V., *J. Phys. Chem. B*, 2005, vol. 109, p. 7451.
44. Phillippi, C.M. and Mazdiyasni, K.S., *J. Am. Cream. Soc.*, 1971, vol. 54, no. 5, p. 254.
45. Gualtieri, A., Norby, P., Hanson, J., and Hriljac, J., *J. Appl. Crystallogr.*, 1996, vol. 29, p. 707.
46. Li, M., Feng, Z., Xiong, G., Ying, P., Xin, Q., and Li, C., *J. Phys. Chem. B*, 2001, vol. 105, no. 34, p. 8107.
47. Perevalov, T.V., Shaposhnikov, A.V., Tapilin, V.M., Nasyrov, K.A., Gritsenko, D.V., and Gritsenko, V.A., in *Defects in High-κ Gate Dielectric Stacks*, NATO Science Series II: Mathematics, Physics and Chemistry, vol. 220, Dordrecht: Springer, 2006, p. 423.
48. Devia, D.H. and Sykes, A.G., *Inorg. Chem.*, 1981, vol. 20, p. 910.
49. Frolova, Yu.V., Sadykov, V.A., Pavlova, S.N., Veniaminov, S.A., Bunina, R.V., Burgina, E.B., Kolomiichuk, V.N., Larina, T.V., Mezentseva, N.V., Fedotov, M.A., Volodin, A.M., Paukshtis, E.A., Fenelonov, V.B., Roy, R., and Agrawal, D., *Mater. Res. Soc. Symp. Proc.*, 2004, vol. 788, p. 215.
50. Kirichenko, O.A., Graham, G.W., Chun, W., and McCabe, R.W., *Stud. Surf. Sci. Catal.*, 1998, vol. 118, p. 411.
51. Rossignol, S., Madier, Y., and Duprez, D., *Catal. Today*, 1999, vol. 50, p. 261.
52. Bozo, C., Gaillar, F., and Guilhaume, N., *Appl. Catal., A*, 2001, vol. 220, p. 69.
53. Letichevsky, S., Tellez, C.A., de Avillez, R., Silva, M.I.P., Fraga, M.A., and Appel, L.G., *Appl. Catal., B*, 2005, vol. 58, p. 203.
54. Kozlov, A.I., Kim, D.H., Yezerets, A., Andersen, P., Kung, H.H., and Kung, M., *J. Catal.*, 2002, vol. 209, p. 417.
55. Terrbile, D., Trovarelli, A., Llorca, J., Leitenburg, C., and Dolcetti, G., *Catal. Today*, 1998, vol. 43, p. 79.
56. Fernandez-Garcia, M., Wang, X., Belver, C., Iglesia-Juez, A., Hanson, J.C., and Rodriguez, A., *Chem. Mater.*, 2005, vol. 17, p. 4181.
57. Shevchenko, V.Ya., Glushakova, V.B., Panova, T.I., Podzorova, L.I., Il'icheva, A.A., and Lapshina, A.E., *Izv. Ross. Akad. Nauk, Neorg. Mater.*, 2001, vol. 37, no. 7, p. 821.
58. Mamontov, E., Egami, T., Brezny, R., Koranne, M., and Tyagi, S., *J. Phys. Chem. B*, 2000, vol. 104, p. 11110.
59. Lemaux, S., Bensaddik, A., van der Eerden, A.M.J., Bitter, J.H., and Koningsberger, D.C., *J. Phys. Chem. B*, 2001, vol. 105, p. 4810.
60. Vlaic, G., Fornasiero, P., Geremia, S., Kaspar, J., and Granziani, M., *J. Catal.*, 1997, vol. 168, no. 2, p. 386.
61. Trovarelli, A., de Leitenburg, C., and Dolcetti, G., *Chem.–Tech.*, 1997, vol. 27, no. 6, p. 32.
62. Mamontov, E., Brezny, R., Koranne, M., and Egami, T., *J. Phys. Chem. B*, 2003, vol. 107, p. 13007.
63. Nagai, Y., Yamamoto, T., Tanaka, T., Yoshida, S., Nonaka, T., Okamoto, T., Suda, A., and Sugiura, M., *Catal. Today*, 2002, vol. 74, p. 225.
64. Sugiura, M., *Catal. Surv. Asia*, 2003, vol. 7, no. 1, p. 77.
65. Vidal, H., Bernal, S., Kaspar, J., Pijolat, M., Perrichon, V., Blanco, G., Pintado, J.M., Baker, R.T., Colon, G., and Fally, F., *Catal. Today*, 1999, vol. 54, p. 93.
66. Bulgakov, N.N., Sadykov, V.A., Lunin, V.V., and Kemnitz, E., *React. Kinet. Catal. Lett.*, 2002, vol. 76, no. 1, p. 111.
67. Cabanas, A., Darr, J.A., Lester, E., and Poliakoff, M., *J. Mater. Chem.*, 2001, vol. 11, p. 561.
68. Chemarin, C., Rosman, N., Pagnier, T., and Lucazeau, G.A., *J. Solid State Chem.*, 2000, vol. 149, p. 298.
69. Strekalovskii, V.N., Makurin, Yu.N., and Vovkotrub, E.G., *Neorg. Mater.*, 1983, vol. 19, no. 6, p. 925.
70. Kharlanov, A.N., Lunina, E.V., and Lunin, V.A., *Zh. Fiz. Khim.*, 1994, vol. 68, no. 4, p. 692.

71. Borchert, H., Frolova, Y.V., Kaichev, V.V., Prosvirin, I.P., Alikina, G.M., Lukashevich, A.I., Zaikovskii, V.I., Moroz, E.M., Trukhan, S.N., Ivanov, V.P., Paukshtis, E.A., Bukhtiyarov, V.I., and Sadykov, V.A., *J. Phys. Chem. B*, 2005, vol. 109, p. 5728.

72. Inaba, H. and Tagawa, T., *Solid State Ionics*, 1996, vol. 83, p. 1.

73. Li, L. and Lin, X., *J. Mater. Res.*, 2001, vol. 16, no. 11, p. 3207.

74. Greenblatt, M., Shuk, P., Huang, W., Dikmen, S., and Croft, M., *Mater. Res. Soc. Symp. Proc.*, 1999, vol. 548, p. 511.

75. Snytnikov, P.V., *Cand. Sci. (Chem.) Dissertation*, Novosibirsk: Inst. of Catalysis, 2004.

76. Zhang, Y., Andersson, S., and Muhammed, M., *Appl. Catal., B*, 1995, vol. 6, p. 325.

77. Turko, G.A., Ivanova, A.S., Plyasova, L.M., Litvak, G.S., Rogov, V.A., Slavinskaya, E.M., Polukhina, I.A., and Noskov, A.S., *Kinet. Katal.*, 2007, vol. 48, no. 1, p. 150 [*Kinet. Catal.* (Engl. Transl.), vol. 48, no. 1, p. 143].

78. Markaryan, G.L., Ikryannikova, L.N., Muravieva, G.P., Turakulova, A.O., Kostyuk, B.G., Lunina, E.V., Lunin, V.V., Zhilinskaya, E., and Aboukais, A., *Colloids Surf., A*, 1999, vol. 151, no. 3, p. 435.

79. Ikrynnikova, L.N., Aksenov, A.A., Markaryan, G.L., Murav'eva, G.P., Kostyuk, B.G., Kharlanov, A.N., and Lunina, E.V., *Appl. Catal., A*, 2001, vol. 210, p. 225.

80. Salomatina, O.V., Kuznetsova, T.G., Korchagina, D.V., Paukshtis, E.A., Moroz, E.M., Volcho, K.P., Barkhash, V.A., and Salakhutdinov, N.F., *J. Mol. Catal. A: Chem.*, 2007, vol. 269, p. 72.